

Turbulence, transport, and zonal flows in the Madison symmetric torus reversed-field pinch

Z. R. Williams, M. J. Pueschel, P. W. Terry, and T. Hauff

Citation: [Physics of Plasmas](#) **24**, 122309 (2017); doi: 10.1063/1.5000252

View online: <https://doi.org/10.1063/1.5000252>

View Table of Contents: <http://aip.scitation.org/toc/php/24/12>

Published by the [American Institute of Physics](#)

Articles you may be interested in

[Observation of trapped-electron-mode microturbulence in reversed field pinch plasmas](#)

[Physics of Plasmas](#) **25**, 010701 (2018); 10.1063/1.5010198

[A theory of self-organized zonal flow with fine radial structure in tokamak](#)

[Physics of Plasmas](#) **24**, 122304 (2017); 10.1063/1.4995302

[Impact of neoclassical tearing mode–turbulence multi-scale interaction in global confinement degradation and magnetic island stability](#)

[Physics of Plasmas](#) **24**, 122503 (2017); 10.1063/1.5004987

[How pattern is selected in drift wave turbulence: Role of parallel flow shear](#)

[Physics of Plasmas](#) **24**, 122305 (2017); 10.1063/1.5001857

[Saturation scalings of toroidal ion temperature gradient turbulence](#)

[Physics of Plasmas](#) **25**, 012308 (2018); 10.1063/1.5007062

[Neoclassical quasilinear theory in the superbanana plateau regime and banana kinetics in tokamaks](#)

[Physics of Plasmas](#) **24**, 122504 (2017); 10.1063/1.4999421

PHYSICS TODAY

WHITEPAPERS

ADVANCES IN PRECISION
MOTION CONTROL

Piezo Flexure Mechanisms
and Air Bearings

READ NOW

PRESENTED BY

PI

Turbulence, transport, and zonal flows in the Madison symmetric torus reversed-field pinch

Z. R. Williams,¹ M. J. Pueschel,¹ P. W. Terry,¹ and T. Hauff^{2,3}

¹*Department of Physics, University of Wisconsin-Madison, Madison, Wisconsin 53706, USA*

²*Jakob-Brucker-Gymnasium, 87600 Kaufbeuren, Germany*

³*Max-Planck-Institut für Plasmaphysik, 85748 Garching, Germany*

(Received 14 August 2017; accepted 28 November 2017; published online 19 December 2017)

The robustness and the effect of zonal flows in trapped electron mode (TEM) turbulence and Ion Temperature Gradient (ITG) turbulence in the reversed-field pinch (RFP) are investigated from numerical solutions of the gyrokinetic equations with and without magnetic external perturbations introduced to model tearing modes. For simulations without external magnetic field perturbations, zonal flows produce a much larger reduction of transport for the density-gradient-driven TEM turbulence than they do for the ITG turbulence. Zonal flows are studied in detail to understand the nature of their strong excitation in the RFP and to gain insight into the key differences between the TEM- and ITG-driven regimes. The zonal flow residuals are significantly larger in the RFP than in tokamak geometry due to the low safety factor. Collisionality is seen to play a significant role in the TEM zonal flow regulation through the different responses of the linear growth rate and the size of the Dimits shift to collisionality, while affecting the ITG only minimally. A secondary instability analysis reveals that the TEM turbulence drives zonal flows at a rate that is twice that of the ITG turbulence. In addition to interfering with zonal flows, the magnetic perturbations are found to obviate an energy scaling relation for fast particles. *Published by AIP Publishing.*

<https://doi.org/10.1063/1.5000252>

I. INTRODUCTION

Anomalous transport driven by microinstabilities is detrimental to the energy and particle confinement in fusion experiments. Strategies to control anomalous transport necessarily require a thorough understanding of these microinstabilities and the turbulence that arises from them. Ion-temperature-gradient-driven (ITG) turbulence and trapped-electron mode (TEM) turbulence arise from two prominent microinstabilities that occur at the ion-gyroradius scales in a large range of fusion devices, including tokamaks,^{1,2} stellarators,³⁻⁵ and reversed-field pinches⁶⁻¹⁰ (RFPs). It has long been recognized that the levels of transport caused by these microinstabilities can be sensitive to zonal flows¹¹⁻¹⁴ through some form of regulation involving shear¹⁵ or energy transfer to the large-scale stable modes.^{16,17}

Recent work has shown that zonal flows are degraded by the radial magnetic field fluctuations,^{18,19} thereby allowing the magnetic fluctuations to affect the levels of the microinstability-driven transport. Because the RFP is subject to magnetic fluctuations associated with the global tearing modes, it is a natural test bed for observing the effects of magnetic fluctuations on the microinstability-driven transport through zonal flows. This paper presents the analysis of TEM and ITG turbulences based on specific RFP discharges in the Madison Symmetric Torus (MST), showing that zonal flows play very different roles in regulating transport for these two instabilities, and seeking reasons for the differences.

Examining TEM and ITG in the RFP provides a regime of critical parameters that is different from tokamaks, and

which elucidates the important physics. Specifically, plasmas in the RFP are characterized by a low safety factor $q \equiv rB_\phi/RB_\theta$ (r is minor radius, R major radius, B_ϕ and B_θ are the toroidal and poloidal fields, respectively), as well as the smaller shear scale lengths (thus larger shear) than those of the tokamaks. It is observed in gyrokinetic simulations discussed in this work that the zonal flow residuals, in particular, are highly sensitive to the value of q , with the RFP's small- q magnetic configuration resulting in a sustained zonal-flow-dominated state in which the transport can be fully suppressed. Such RFP simulations are highly idealized because they neglect the tearing mode fluctuations, which are unstable in RFP discharges, and therefore available for disrupting zonal flows and raising transport.⁹ Acquiring a better understanding of this idealized state is desirable for clarifying the role of zonal flows in transport regulation for certain microinstabilities.

In the MST experiment, large-scale tearing modes cannot be eliminated entirely. However, the effects of tearing modes can be mitigated to a significant degree by operating the MST with a modification to the Ohmic drive called Pulsed Poloidal Current Drive (PPCD),²⁰ in which a poloidal current is induced in the edge of the plasma. This flattens the current profiles and consequently lowers the tearing mode drive, significantly reducing the stochastic transport and improving confinement in the MST to tokamak-like levels.²¹ Operating in PPCD has allowed new investigations of RFP physics, both computational and experimental. Prior gyrokinetic work⁹ showed that TEM and ITG microturbulences can contribute significantly to transport in PPCD, possibly fixing the edge pressure gradient at a critical value. Additionally,

Ref. 9 first identified the zonal-flow-dominated state at outer radii in the absence of tearing fluctuations for discharges unstable to TEM and provided the initial results on the effect of radial magnetic fluctuations on that state.

The simulations described herein show that the effect of the radial magnetic fluctuations in MST varies with the driving instability. In TEM turbulence, the introduction of an ad-hoc tearing parity magnetic field perturbation at the nominal level of tearing mode fluctuations in PPCD discharges significantly reduces zonal flows and raises the TEM heat flux to levels consistent with the experiment. In ITG turbulence, the effect is far less substantial, with flux levels that increase by tens of percent instead of orders of magnitude. Experimentally, recent work²³ has detailed the measurements of density fluctuations attributed to the TEM microturbulence in a recent set of PPCD discharges, and for the first time such observations have been reported in the RFP. The focus of the present work is to gain a deeper understanding of the physics with particular emphasis on the role zonal flows play in the TEM and ITG turbulences in MST PPCD discharges.

Two specific PPCD discharges are studied in this work, characterized by their ratio of temperature gradient to density gradient η outside the reversal surface. For one discharge, TEM is the dominant instability; ITG is the primary instability in the second. The turbulence generated by these instabilities in their respective discharges is examined, both in the idealized, tearing-free regime, as well as in the regime including the residual tearing effects. The TEM turbulence in the tearing-free configuration is dominated by strong zonal flows, which suppress all flux at nominal experimental gradients. The strong zonal flows also appear in the ITG-dominated discharge; however, there is still a finite flux generated by the turbulence (although still much less than that seen in the experiment). The strong zonal flows seen in tearing-free simulations of both discharges can be attributed, at least partially, to the RFP's low- q magnetic configuration. The difference in transport between TEM (no flux) and ITG (finite flux) in this idealized regime is addressed by comparing the influence of collisionality, as well as the dynamics of secondary instability, between the two discharges. The inclusion of tearing fluctuations serves to degrade zonal flows in both cases, although the effect on transport driven by the different instabilities varies significantly, as mentioned earlier. As an additional probe of magnetic fluctuation effects on turbulence, we consider the fast ion transport in the RFP. It is observed that in the absence of magnetic tearing fluctuations, the fast ion energy diffusivity scaling matches very well the theoretical predictions made previously for tokamaks,²² while the inclusion of tearing fluctuations establishes a separate regime to which this theory does not apply.

This work is organized as follows: Sec. II provides the experimental framework and measurements that originally motivated the subsequent numerical studies, as well as a discussion of the linear simulations performed to describe the dominant instabilities for the two specific PPCD discharges. In Sec. III, the turbulence generated in each of these discharges and its response to tearing fluctuations are described in detail. An analysis of the multiple contributing processes

to the unique zonal flow behaviors seen in these discharges is presented in Sec. IV. Section V describes the effect that the tearing perturbations in MST have on the energetic particle diffusivities, and how they compare with the tokamak-based expectations. The results are summarized in Sec. VI.

II. CHARACTERIZATION OF MICROTURBULENT FLUCTUATIONS IN MST

Prior gyrokinetic modeling of the MST microinstability properties⁹ focused on two different PPCD discharges, with different values of the toroidal current induced in the plasma. That work examined discharges with toroidal plasma currents of 200 and 500 kA, which exhibited dominant instabilities of ITG and density-gradient-driven TEM, respectively. Recent work using an updated FIR system has produced measurements for new 200 kA PPCD discharges of deuterium plasmas, around which the present work is centered. The FIR diagnostic was used to measure density fluctuations during PPCD discharges;²³ the measurements show that as the induced poloidal current grows in PPCD, the large-scale tearing mode amplitudes decay until reaching some small, quasi-stationary value. In the PPCD “flat top,” where the tearing modes are maximally (but not fully) suppressed, a steepening of the density gradient was observed, accompanied by higher-frequency density fluctuations. This steepening of density (and temperature) profiles occurs primarily outside the reversal surface (the flux surface where $B_\phi = 0$ and thus $q = 0$). Inside the reversal surface, the profiles remain relatively flat. Consequently, the high-frequency density fluctuations are observed almost entirely in this outer region.

Experimental scans show a strong dependence of these fluctuations on the density gradient, with a critical gradient $R_0/L_n \approx 10$, where R_0 is the major radius on axis ($R = R_0 + r \cos \theta$, where θ is poloidal angle), $L_n^{-1} \equiv (1/n_0) dn_0/dr$ is the equilibrium density gradient scale length, and n_0 is the background plasma density. The fluctuations are observed to propagate in the electron diamagnetic direction in the perpendicular wavenumber range $k_\perp \rho_s \lesssim 0.2$. The measurements of carbon impurity density fluctuations in PPCD using ion Doppler spectroscopy (IDS), performed in parallel with FIR, also observed fluctuations in the 50–100 kHz frequency range outside the reversal surface,²⁴ providing evidence that the fluctuations are due to TEM.

In an effort to understand the underlying nature of these fluctuations, gyrokinetic simulations based on the experimental profile data from the new 200 kA PPCD discharges discussed earlier were performed at four different radial locations in the range $0.55 < r/a < 0.85$, focusing primarily outside of the reversal surface (located at $r/a \approx 0.7$) where the high-frequency density fluctuations were observed. All simulations discussed in this paper are local flux-tube calculations performed using the Gene code^{25,26} with RFP-specific equilibrium modifications implemented via the Adjusted Circular Model (ACM).⁹ The latter expands upon the standard Circular model of circular concentric flux surfaces²⁷ to account for the magnetic field variation with minor radius intrinsic to the RFP.

TABLE I. Physical parameters taken from MSTFit equilibrium reconstructions of 200 kA PPCD discharges and used as input for Gene simulations. $R_0/L_T = R_0/L_{Te} = R_0/L_{Ti}$ and $T_{i0} = 0.4T_{e0}$.

| Instability | r/a | q | \hat{s} | β | ν_c | R_0/L_T | R_0/L_n |
|-------------|-------|---------|-----------|---------|---------|-----------|-----------|
| TEM | 0.565 | 0.0528 | -6.05 | 0.11 | 0.0029 | 9.67 | 4.79 |
| | 0.748 | -0.0690 | 8.16 | 0.028 | 0.0088 | 23.6 | 23.0 |
| | 0.791 | -0.103 | 6.18 | 0.014 | 0.013 | 28.9 | 28.5 |
| | 0.836 | -0.141 | 5.00 | 0.0053 | 0.020 | 37.1 | 34.2 |
| | 0.807 | -0.1103 | 5.08 | 0.0063 | 0.27 | 30.0 | 19.1 |
| ITG | 0.807 | -0.1103 | 5.08 | 0.0063 | 0.27 | 30.0 | 19.1 |

Nominal resolutions for these simulations were 16 grid points in the direction parallel to the magnetic guide field, 32 parallel velocity grid points, and 8 magnetic moment grid points; the linear simulations required $15k_x$ modes (where k_x refers to radial wavenumber). The profiles used as input for the code were obtained from an MSTFit²⁸ equilibrium reconstruction. Specific input parameters used in this work are listed in Table I. As discussed in Ref. 9, radial locations near the reversal surface are numerically more challenging, because the parameter $\hat{s} \equiv (r/q)dq/dr$, which represents shear in a tokamak, diverges at the $q=0$ surface. In the RFP, the magnetic shear remains well-behaved throughout the plasma volume, and the physics of the simulations is unaffected by the behavior of \hat{s} near $q=0$. However, \hat{s} is used in Gene for the flux-tube boundary conditions and as a metric for dq/dr . The microturbulent fluctuations detected in the experiment were localized sufficiently far from the reversal surface to support the assumption that the exclusion of the region near the reversal surface in the present work does not significantly alter its relevance.

Inside the reversal surface, the equilibrium profiles are mostly flat, and thus the plasma is stable to microinstability throughout almost the entire region. There is a strong linear destabilization outside the reversal surface ($r/a \gtrsim 0.7$). This radial localization of instability matches the FIR measurements, which detected high-frequency density fluctuations primarily outside the reversal surface. Such strong destabilization is attributed to the large background density and temperature gradients, which form in that region during PPCD. Precise data on ion temperature profiles $T_{i0}(r)$ is lacking for these discharges, so it is assumed that $T_{i0} \approx 0.4T_{e0}$ at all radii, and the normalized temperature gradients of both species are the same; the density gradients are equal for ions and electrons due to quasineutrality. A consequence of these assumptions is that $\eta_i = \eta_e = \eta$, where $\eta_j \equiv (d \ln T_{j0}/dr)/(d \ln n_{j0}/dr)$. For this discharge, $\eta \approx 1.0$ outside the reversal surface. A common empirical rule²⁹ developed from the tokamak gyrokinetic simulations, which has also been found to apply to the RFP,⁹ states that $\eta \approx 1.3$ defines a boundary between ITG- and TEM-dominated regimes, with $\eta \lesssim 1.3$ being TEM-dominated.

As seen in Fig. 1, the dominant instability propagates at the toroidal wavenumbers $0.1 \leq k_y \rho_s \leq 1$, in the electron diamagnetic direction (denoted by negative frequencies). The transition to positive frequencies at higher k_y is a feature of the so-called ubiquitous TEM.³⁰ Scans were performed separately for density, ion temperature, and electron temperature gradient at $k_y \rho_s = 0.5$, where the linear growth rate peaks. Each quantity was scanned over a range of values, while all other parameters were held fixed at their experimental values. As shown in Fig. 1, at experimental parameters the linear growth rate varies most strongly with the density gradient, agreeing with the expectation of a density-gradient-driven

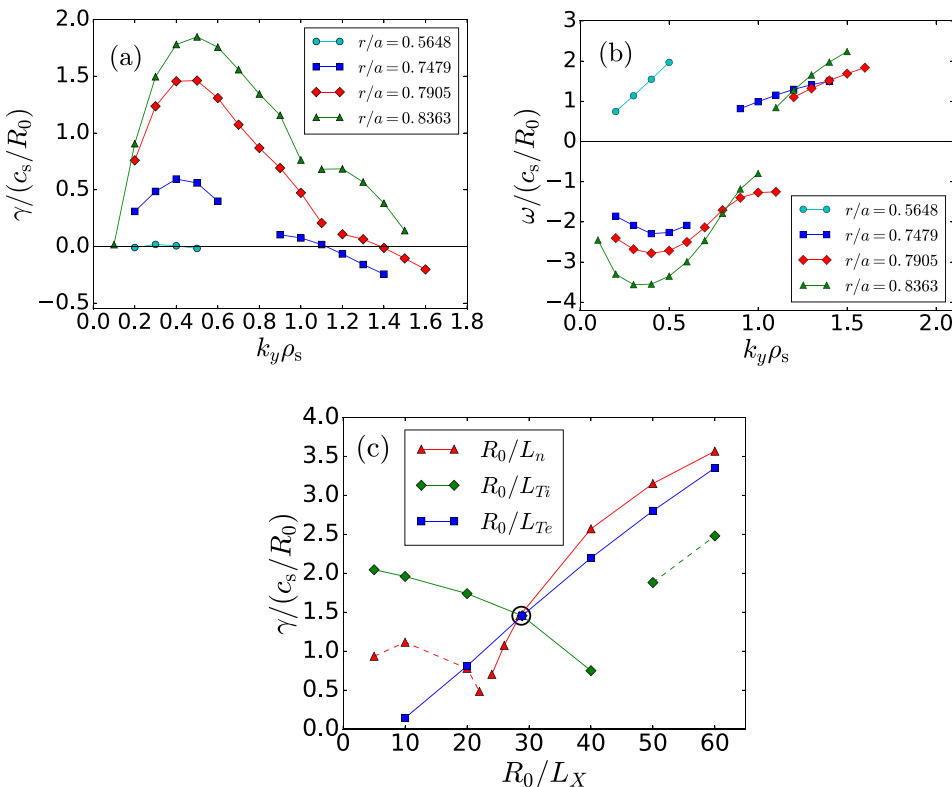


FIG. 1. Linear instability analysis for the low- η , 200 kA PPCD. In (a), growth rates are strongest in the $k_y \sim 0.1-1$ range. In (b), dominant frequencies are in the electron diamagnetic direction, with positive branches arising from the ubiquitous TEM. In (c), gradient scans at $k_y \rho_s = 0.5$ and $r/a = 0.7905$ are shown, with experimental values circled. The three solid-line curves correspond to variation of the density gradient (triangles), ion temperature gradient (diamonds), and electron temperature gradient (squares) with other gradients held fixed. The density-gradient drive is the strongest for nominal parameters. Dashed lines correspond to a separate, ion-direction unstable mode branch.

trapped-electron mode. To provide further support of this assessment, the linear analysis was repeated, separating the contributions of trapped and passing particles. As seen in Fig. 2, the cross phases between the electrostatic potential and the electron density fluctuations reveal that the trapped electrons exhibit a phase difference of $\approx +\pi/2$, consistent with instability, while the corresponding passing-electron fluctuations are primarily in phase.

As a point of comparison with the TEM characterization, a linear analysis was performed on another recent 200 kA PPCD discharge in which the background temperature gradients are $\approx 50\%$ larger than the background density gradients. The increased temperature gradients result in $\eta \approx 1.5$, characteristic of an ITG-dominated regime. The dominant instability in this case propagates in the ion diamagnetic direction at wavenumbers of $k_y \rho_s \sim 0.1 - 1$. Figure 3 shows the instability being driven strongly by the ion temperature gradient, and stabilized by both the electron temperature gradient and the density gradient. These qualities are consistent with the ITG instability, as expected for $\eta > 1.3$. In what follows, the nonlinear behavior of these two instabilities in the RFP are compared.

III. GYROKINETIC TURBULENCE IN PPCD

Turbulence and transport in PPCD discharges are modeled using nonlinear flux-tube simulations. The RFP has a large magnetic shear, varying on the minor radius scale, which can result in significant nonlinear simulation costs, as modes with very different radial scales (very different k_x)

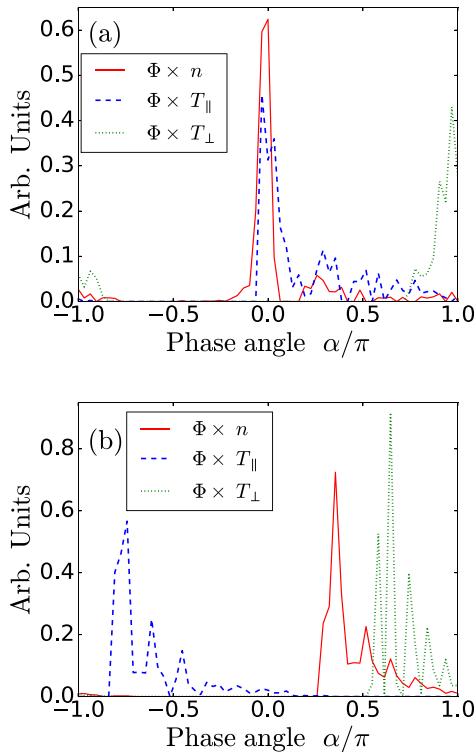


FIG. 2. Cross phases constructed from fluctuating quantities (Φ , n , T_{\parallel} , and T_{\perp}) for passing electrons in (a) and trapped electrons in (b). The phase difference $\alpha \approx +\pi/2$ between Φ and n corresponds to a ∇n -driven instability, and only arises from the trapped-particle distribution.

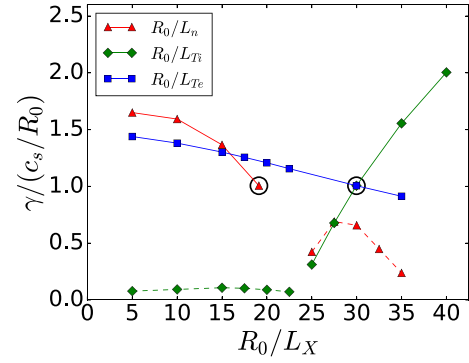


FIG. 3. Gradient scans at $k_y \rho_s = 0.5$ and $r/a = 0.807$ for the high- η PPCD discharge, with experimental values circled. The three solid-line curves corresponding to variation of the density gradient (triangles), ion temperature gradient (diamonds), and electron temperature gradient (squares), with other gradients held fixed. Consistent with ITG modes, the ion temperature gradient R/L_{Ti} strongly destabilizes the mode, while the electron temperature and density gradients have a stabilizing effect. Dashed lines correspond to a separate, electron-direction mode branch.

become coupled through the flux-tube parallel boundary condition. The highest-magnitude shear value considered in the nonlinear simulations is $\hat{s} = 6.18$, for which the numerical convergence requires a total of 192 (positive and negative) k_x Fourier modes when resolving the k_y spectrum with 12 modes. The perpendicular box has an extent of $16 \rho_s$ in the radial x direction, and $31.4 \rho_s$ in the y (toroidal-like) direction. The following discussion focuses on the results from nonlinear simulations at $r/a = 0.8$.

Nonlinear calculations based on the TEM-dominated discharge produced negligible transport, with the electrostatic heat diffusivity of order $\chi_e \sim 10^{-4} \text{ m}^2/\text{s}$. This is a consequence of very strong zonal flows seen in Fig. 4(a), which are generated nonlinearly, overcoming any linear instability drive, suggesting that there is physics present in the experiment that these simulations do not capture. Indeed, the simulations do not take into account the background current

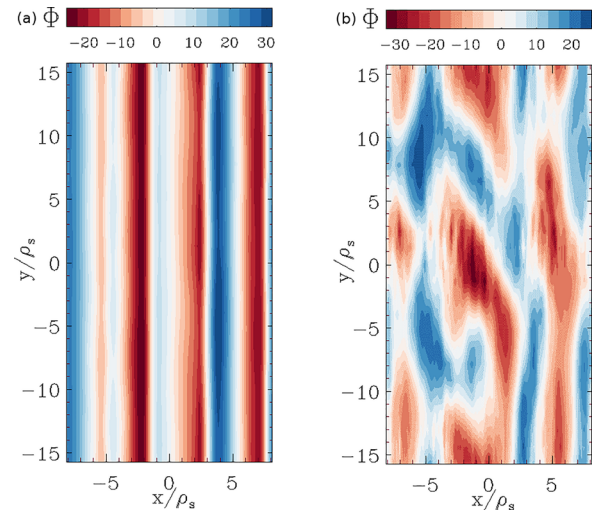


FIG. 4. Electrostatic potential contours Φ (in units of $\rho_s e / (R_0 T_e)$) in TEM turbulence for simulations with zero (a) and finite (b) residual magnetic tearing fluctuations. In the absence of magnetic activity associated with tearing modes, TEM instability leads to very strong zonal flow formation and the complete suppression of heat and particle transport.

gradients, which drive the tearing modes primarily in the core of the RFP. Though reduced in PPCD, these tearing fluctuations play an important role in setting microturbulent transport levels.⁹ To self-consistently model the tearing mode effects, the current gradients would need to be included in a global simulation combining the core and edge regions. In lieu of using fully global simulations to model these residual tearing fluctuations, an ad-hoc tearing-parity, constant-in-time A_{\parallel} perturbation is implemented in the code. For details on the perturbation, which has been modified from that used in Ref. 9, see the Appendix.

The inclusion of this perturbation degrades the previously very strong zonal flow activity, shown in the electrostatic potential contours in Fig. 4(b). As detailed in Ref. 18, the radial magnetic field perturbation allows the electron streaming along field lines to travel to different flux surfaces, effectively sorting out the electrostatic potential differences and thus degrading the zonal flows. The impact of this process can be described quantitatively by determining the difference in the linear and nonlinear critical gradients, as shown in Fig. 5 (this upshift in the critical gradient is referred to as the Dimits shift³¹). While the case of without tearing fluctuations experiences a factor of four upshift in critical density gradient, the inclusion of fluctuations removes the upshift almost entirely.

This zonal flow degradation results in increased transport values. Setting the strength of the perturbation based on the magnetic field measurements taken at the wall, the calculated diffusivity ($\chi_e \approx 10 \text{ m}^2/\text{s}$) comes to within 30%

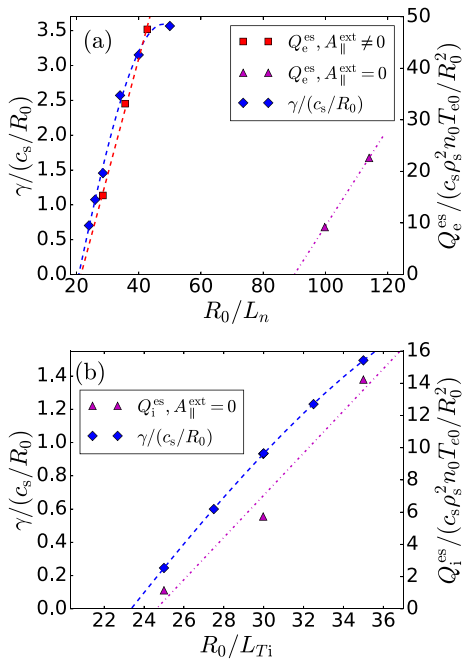


FIG. 5. Linear growth rates and heat fluxes (in units of $c_s \rho_s^2 n_0 T_{e0}/R_0^2$) vs. driving gradients. Diamonds correspond to linear growth rates, triangles to heat fluxes without the tearing perturbation imposed, and squares to heat fluxes with the imposed tearing perturbation. In (a), for TEM without magnetic perturbations modeling tearing mode effects, the linear (blue diamonds) and nonlinear (magenta triangles) critical gradients differ by a factor of four. With tearing (red squares), they nearly coincide. In (b), even without tearing activity, there is almost no difference between linear and nonlinear critical gradients in the ITG case.

agreement with that expected from the experimental data. It is important to note that transport, both here and throughout this work, refers only to the electrostatic transport resulting from radial $E \times B$ flows. There is also the magnetic flutter transport that increases with the tearing perturbation as one would expect, which is observed in simulations to be of the same order as the electromagnetic transport for the experimentally relevant parameters. The method in which the tearing fluctuations are accounted for is not self-consistent, thus conclusions concerning the physics of electromagnetic transport cannot be drawn from this work; as such only transport through the electrostatic channel is examined.

It is interesting to note that while both the ITG- and TEM-dominated discharges generate zonal flows, only in the TEM case the transport is affected so severely. In the absence of tearing fluctuations, the ITG-dominated simulation at the experimental gradients still exhibits finite transport, despite also establishing prominent zonal flows. Including the tearing perturbation results in only a slight increase in fluxes for ITG, depicted in Fig. 6. It should be noted that zonal flows are still degraded by the tearing perturbation in the ITG case, exhibiting a change in zonal flow structure comparable to that seen in Fig. 4 for the TEM case. Additionally, the Dimits shift in the ITG case is very small compared to the TEM case as well as standard tokamak cases, even in the absence of tearing fluctuations.

In an ITG simulation which removes contributions from the zonal flows (zeroing out the flux-surface-averaged electrostatic potential Φ), the increase in the flux is of the same order as that seen in the case in which the tearing fluctuations degrade the zonal flow (factor of 2 increase in flux when the tearing perturbation is applied vs. factor of 3 increase when zonal Φ contributions are removed). This suggests that in this ITG-dominated discharge, the saturation does not rely on zonal flows nearly as much as in the TEM case (in which both the tearing perturbation and the removal of zonal Φ result in orders of magnitude transport increase).

This contrasts sharply with the tokamak gyrokinetic simulations, which show that zonal flows play a significant role in the ITG turbulence saturation. There is evidence that this notable difference is rooted in the branch of the unstable

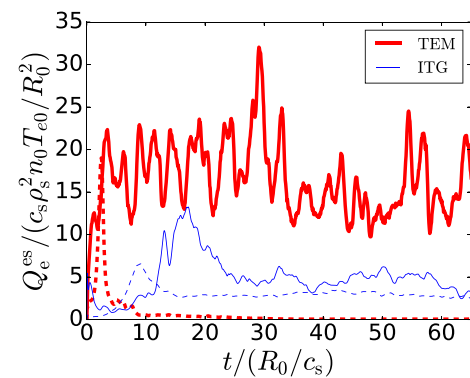


FIG. 6. Electrostatic heat flux time traces, with (solid) and without (dashed) a magnetic perturbation modeling tearing modes. TEM transport (thick lines) is increased by orders of magnitude, while ITG transport (thin lines) only changes by approximately a factor of two, despite imposing an identical tearing perturbation.

ITG mode favored by the equilibrium and the corresponding type of mode coupling interaction that dominates the saturation. In the tokamak, the ITG instability comes in two varieties, a so-called sheared-slab ITG branch with a mode structure that is flute-like and governed by a magnetic shear, and a toroidal branch with a ballooning mode structure governed by a magnetic curvature.³² Which branch is favored depends on the relative magnitudes of the parallel and curvature drift frequencies. In the slab ITG branch, mode coupling between the unstable ITG mode and a conjugate stable mode that dominates saturation is mediated by a marginally stable eigenmode.³³ In the toroidal branch, a balance of parallel flow with the shear, the poloidal variation, and the radial wave propagation removes the marginal mode from the linear eigenmode spectrum.³² Mode coupling then favors a saturation channel that uses the zonal flow, thereby introducing zonal-flow regulation,^{16,17,34} The gyrokinetic simulations of ITG turbulence in a stellarator support this picture of mode coupling. Zonal flows have a significant impact on saturation when the toroidal branch dominates. When the shear is strengthened only enough to bring the parallel and curvature drift frequencies to comparable values, the zonal flow no longer dominates saturation.³⁵ Instead, removing the zonal flows results in only a slight increase in saturation level, much like the situation described here for the ITG turbulence in the RFP. Moreover, an analysis of the triplet wavenumber interactions further confirms that non-zonal couplings become dominant in the regime of comparable drifts.

The parameter that delineates the two branches of ITG instability is the ratio of the scale lengths of the magnetic shear to the magnetic curvature L_s/κ^{-1} , where $\kappa \approx \nabla_{\perp} B/B$ in a low- β plasma. For $L_s/\kappa^{-1} < 1/2$ the mode is shear-slab-like, while in the opposite limit it is a curvature dominated mode.³²

For tokamaks, L_s is given by the well known formula $L_s = Rq/\hat{s}$ where $\hat{s} = (r/q)dq/dr$. In the RFP, the comparable magnitudes of the toroidal and poloidal fields invalidate the tokamak expression for shear in the outer half of the plasma, and instead $L_s = r/(Rdq/dr)$. It should also be noted that the magnetic field curvature that dominates in most of the plasma volume of the RFP is the poloidal-field curvature.

For the ITG-dominated discharge the shear and curvature scale lengths were $L_s = 0.21\text{m}$ and $\kappa^{-1} = 0.47\text{m}$, making $L_s/\kappa^{-1} = 0.45$. This places the plasma at the cross between the two ITG branches, and critically, from the arguments given earlier indicates that zonal flows do not play a dominant role in saturation.

These results are also consistent with an analysis of parallel mode structure as quantified by $c_s k_{\parallel}/\omega$, where $c_s = (T_e/m_i)^{1/2}$ is a characteristic sound speed, k_{\parallel} is a parallel wavenumber calculated from the width of the mode along the field, and ω is the linear frequency of the mode. For ITG modes dominated by curvature one expects localized mode structure with k_{\parallel} large, or $c_s k_{\parallel}/\omega > 1$, while for modes dominated by shear one expects a more extended structure with $c_s k_{\parallel}/\omega < 1$. For the ITG instability discussed in this work $c_s k_{\parallel}/\omega \approx 0.3$, while $c_s k_{\parallel}/\omega \approx 1.1$ for Cyclone Base Case (CBC) parameters.³¹

IV. ZONAL FLOW CHARACTERIZATION

To model the MST experiment, it is necessary for microturbulence models to incorporate tearing perturbations. Because tearing mode suppression is a goal of current profile control in the RFP, the behavior of zonal flows and turbulence observed in the absence of tearing modes is worth investigating. In particular, if the RFP could operate with full tearing suppression, it would likely be able to sustain much steeper gradient profiles relative to tokamaks, thus enhancing its performance.³⁶ In light of the preceding discussion, there are two properties of these RFP discharges that merit investigation: (1) the ability (in the absence of tearing modes) to support very strong zonal flows, and (2) the fact that zonal flows play very different roles in saturation for the ITG and TEM discharges. The first point is addressed by examining the Rosenbluth-Hinton zonal flow residual for RFP geometries. The second point is addressed through examining collisional effects and secondary instability drive.

A. Rosenbluth-Hinton residual

One aspect of the zonal flow behavior is the residual, described in Ref. 38. The plasma responds to an impulsive electrostatic potential on a flux surface through a shielding process in which geodesic acoustic modes driven by the perturbation are damped away and the system arrives at a new constant amplitude Φ_{res} , called the *zonal flow residual*.³⁷ The amplitude of this residual is

$$\frac{\Phi_{\text{res}}}{\Phi_0} = \frac{1}{1 + 1.6q^2/\epsilon_t^{1/2}}, \quad (1)$$

where Φ_0 is the initial amplitude of the electrostatic potential, and $\epsilon_t \equiv r/R_0$. This equation can be thought of as a measure of the ability of the plasma to maintain a zonal-flow amplitude set by a perturbation. The associated physics has been characterized extensively through the numerical simulation see, e.g., Ref. 37. For the magnetic geometry of the present discharges, Fig. 7 shows that the residual is measured to be considerably larger than what is seen in the Cyclone Base Case (CBC), a standard tokamak parameter set, and is

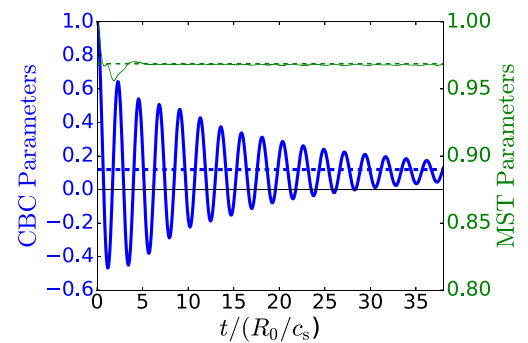


FIG. 7. Electrostatic potential Φ/Φ_0 decay to the zonal flow residual, in good agreement with Eq. (1) for both MST parameters (thin green line, right axis) and CBC (thick blue line, left axis). The small q of the RFP results in a much larger residual value. This calculation was performed at zonal flow wavenumbers of $k_x \rho_s = 0.05$ for the CBC and $k_x \rho_s = 0.3881$ for MST.

still well predicted by Eq. (1). The RFP's low toroidal magnetic field leads to a safety factor q that is at least an order of magnitude smaller than that of the tokamak, resulting in the significantly larger residual. This behavior had been noted previously in the context of RFX-Mod discharges.¹⁰

Figure 8 shows that despite the large residual, Eq. (1) is accurate across a large range of q values, illustrating that it applies to both tokamak and RFP regimes. Large residuals are a contributor to the strong zonal flows seen in simulations. It is important to note that the large zonal flow residuals discussed here apply to plasmas with perfect axisymmetric flux surfaces; experimental reality is better described by including the residual tearing fluctuations. As discussed in Ref. 16 and in Sec. III, the presence of resonant magnetic fluctuations, such as those arising in MST from the residual tearing modes, serves to reduce the zonal flow amplitudes. For more details on the impact of the electromagnetic effects on the zonal flow residuals, see Ref. 17.

While the large zonal flow residuals are consistent with the strong zonal flows seen for simulations unaffected by the tearing modes, they fail to distinguish between turbulence regimes governed by different instabilities and thus provide no information concerning the difference between the TEM and ITG zonal flow activity. Such differences are discussed in Sec. IV B and IV C.

B. Collisionality

In tokamaks, TEM turbulent amplitudes have been observed to vary with collisionality.⁴¹ In particular, higher electron-ion collisionality in a plasma will lead to an increase in electron detrapping, reducing TEM growth rates. Increased collisionality also erodes zonal flows. However, the zonal-flow erosion is less pronounced than the growth rate reduction. Consequently, the balance of the growth rate to the zonal flow level is affected, leading to proportionally stronger zonal-flow regulation as the fluctuations decrease. The effect of collisionality on TEM and ITG modes in the RFP is shown in Fig. 9, where trends similar to those in tokamaks are evident for TEM-dominated discharges. Figure 9(a) shows that when the collisionality is raised from half its nominal experimental value to the experimental value ν_c , the growth rate decreases by 50%. Note that $\nu_c \equiv (R_0/4v_{Te})\nu_{ei}$,

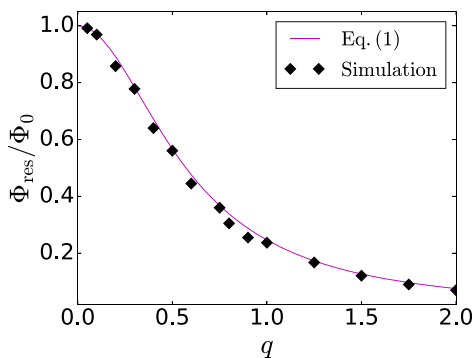


FIG. 8. Scaling of zonal flow residual with safety factor q , showing applicability of Eq. (1) for both tokamak ($q \geq 1$) and RFP ($q \ll 1$) regimes, performed at $k_x \rho_s = 0.3881$ and $\epsilon_t = 0.2741$.

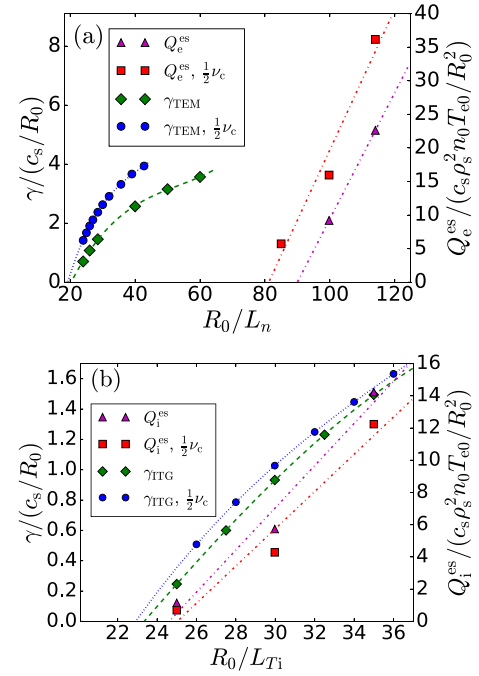


FIG. 9. Linear growth rate and heat flux over a range of driving gradients at nominal and half nominal ν_c . From this, one can measure the Dimits shift change with respect to collisionality for (a) TEM and (b) ITG. Increasing collisionality results in an increase of the Dimits shift in TEM, but no significant change for ITG.

where v_{Te} is the electron thermal speed and ν_{ei} is the electron-ion collision frequency in units of Hz.

However, despite an increase in zonal flow damping, the Dimits shift increases [as made evident by the increased critical gradient for Q_e^{es} in Fig. 9(a)], suggesting that the effect of collisions on the zonal flow is weaker than their effect on the growth rate. This is confirmed by examining how zonal flow residuals and linear growth rates are affected by collisionality. For the TEM case, a factor of two increase in collisionality (from half the experimental value to its full value) results in a 40% reduction of linear growth rates, but only a 30% increase in the zonal flow decay rate, consistent with the results as shown in Fig. 9. These results indicate that the transport regulation of TEM turbulence is increased in a more collisional plasma.

In contrast, Fig. 9(b) shows that collisionality has little effect on either the ITG growth rate or the heat flux. For this case, doubling collisionality causes the zonal flow decay rate to increase by 25% and the linear growth rate to decrease by 10%. The lack of change in ITG Dimits shift is consistent with the previously discussed observations that zonal flows play a less important role in turbulence saturation for the ITG discharge, with collisions working analogously to the tearing fluctuation as a source of zonal flow degradation.

The specific MST data sets analyzed in this work have plasma densities comparable to typical tokamak discharges, but lower temperatures (core $T_{e0} \approx 500 - 600$ eV), leading to a higher collisionality $\nu_c \sim 10^{-1} - 10^{-2}$. For comparison, typical collisionalities in tokamak gyrokinetic simulations² in the region of interest ($r/a \approx 0.8$) are at most $\nu_c \sim 10^{-3}$. This high-collisionality regime of operation thus contributes to the strong zonal-flow suppression of TEM turbulence

observed in simulation by increasing the Dimits shift, while having little effect on ITG turbulence.

C. Secondary instability

Secondary instability analysis describes the process by which a linear instability (e.g., TEM or ITG) causes the excitation of a secondary instability via nonlinear coupling.^{39,40} The secondary instability growth rate is a measure of nonlinear zonal flow excitation strength. Specific details on the procedure for secondary instability analysis are given in Ref. 42. To summarize, a streamer ($k_x = 0$, finite k_y) representing the typically fastest growing linear eigenmode is allowed to evolve linearly with a sideband (both k_x and k_y finite, not connected to the streamer via the parallel flux tube boundary condition) and a zonal flow, until the mode is converged. That state is then used as an initial condition in a subsequent simulation where the linear drive term is set to zero and the streamer is held fixed in time. The nonlinear interaction in the streamer-sideband-zonal-flow triplet results in exponential growth of the secondary mode, here the zonal flow. A secondary growth rate can then be calculated.

The parametric dependencies of the secondary growth rate are studied using scans over magnetic shear \hat{s} and radial wavenumber $k_x \rho_s$, shown in Fig. 10. For experimentally relevant parameters (denoted in the figure by circled points), the TEM secondary growth rate is more than twice that of the ITG secondary. This underscores that in the TEM case, the zonal flow drive is too strong for turbulence to fully

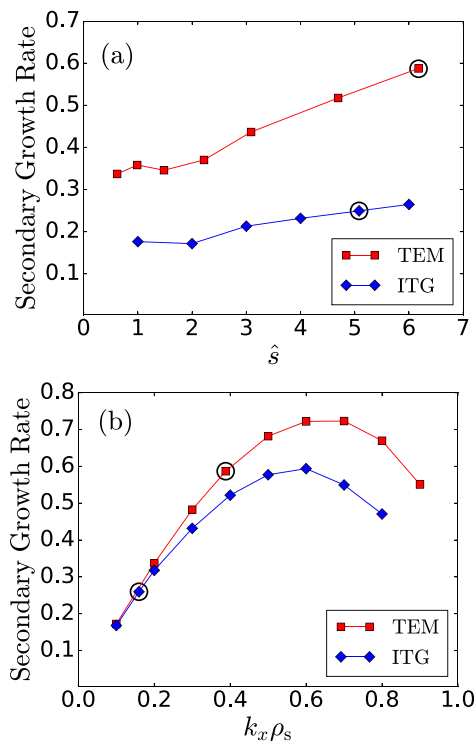


FIG. 10. Secondary growth rate vs. background magnetic shear (a) and radial wavenumber (b) for the two discharges of interest. For default experimental parameters (circled points), the zonal flow secondary growth rate in the TEM case (red squares) is more than two times larger than in the ITG case (blue diamonds), in agreement with the observation of stronger zonal structures for the TEM discharge.

develop, while in the ITG case, a comparable balance between zonal flow and turbulence is maintained. While Fig. 10(b) shows the TEM and ITG secondary growth rates peaking at the same radial wavenumber, in nonlinear simulations, TEM turbulence preferentially generates zonal flows at larger $k_x \rho_s$ than ITG. Figure 11 further illustrates this preference in TEM for smaller radial zonal structures, showing the zonal flow spectra taken from nonlinear simulations. Higher- k_x zonal flows can result in a more effective regulation of turbulence, either through increased eddy shearing or a larger rate of nonlinear energy transfer to damped modes (both of which scale as k_x^2). The reason for the predilection for higher-wavenumber zonal flows in TEM turbulence remains an open question for further study.

V. ENERGETIC PARTICLES IN MST

The question whether microturbulence plays an important factor in fast particle—particularly beam ion—losses in tokamaks has not definitively been answered.^{43–46} One approach in this area is to study decorrelation of fast particles from the microturbulence and calculate the resulting losses,^{22,47} deriving scaling laws for diffusion as a function of particle energy. Notably, the assumptions made in these derivations hold in RFP geometry and should thus apply to MST fast ion diffusion at the radial locations where TEM or ITG microturbulence dominates. While these regions are not studied experimentally with respect to fast particles, they provide an interesting testing ground for theory-simulation comparison. The theory describes fast particle diffusivity in three regimes defined by the pitch angle parameter $\eta_t \equiv v_{\parallel}/v$: trapped particles ($\eta_t \rightarrow 0$), large- ρ_s passing particles ($\eta_t \lesssim 0.9$), and fully passing particles ($\eta_t \rightarrow 1$). Based on Ref. 47, the expected diffusivity scaling with energy for these cases are $D(E) \propto E^{-3/2}$ for trapped and large- ρ_s passing particles and $D(E) \sim E^{-1}$ for fully passing particles.

The simulations including fast deuterium ions ($T_{i0} = 50T_{e0}$) were performed on the TEM-dominated discharge to study diffusivity in RFP conditions. In the tearing-free simulations, the density gradient was increased by a factor of four to go beyond the Dimits regime and permit turbulence to fully develop. As shown in Fig. 12, the diffusivity

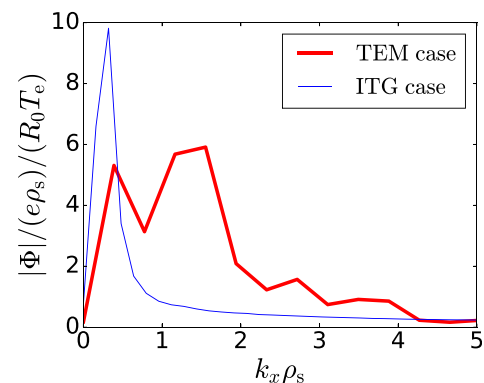


FIG. 11. Zonal flow amplitude spectra from nonlinear simulations, time-averaged over the quasi-stationary state. The zonal flows in the TEM case (thick red line) manifest at higher radial wavenumber than those in the ITG case (thin blue line).

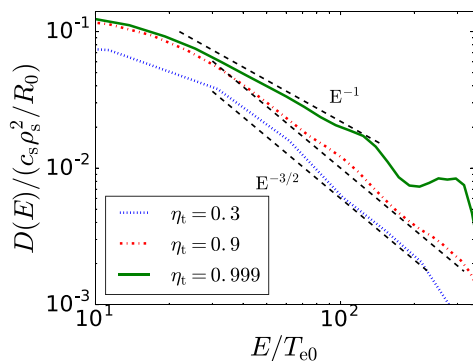


FIG. 12. Electrostatic particle diffusivity for $T_{f0} = 25$ keV fast ions in the TEM-dominated discharge at $r/a = 0.8$ at different pitch angles, with the density gradient increased by a factor of four from the nominal value to allow for turbulent fluctuations in the absence of imposed tearing fluctuations. The dashed lines represent the scaling predicted by theory, with the red and blue curves correspond to $E^{-3/2}$, the green to E^{-1} . It is seen here that the theory works well over a range of particle energies for electrostatic transport in the tearing-free regime.

matches well the expected electrostatic diffusivity scaling for different values of η_t . The lower-energy fast particles ($E \approx 10T_{e0}$), which have been speculated to be most strongly affected by microturbulence,⁴⁴ have diffusivities one to two orders of magnitude less than seen for tokamak cases studied previously,⁴⁷ even despite the large gradients used. The inclusion of an external magnetic perturbation modeling tearing fluctuations violates assumptions on which the theory²² is built. As a result, the diffusivity scaling seen in simulations differs significantly from theoretical expectations across all values of η_t . The next step for the RFP turbulence studies will be multi-scale, accounting for the effect that self-consistently evolved tearing modes in the core have outside the reversal surface. This should resolve the appropriate magnetic fast ion dynamics and hopefully provide insight into these discrepancies.

VI. SUMMARY

Microturbulence in the MST reversed-field pinch has been studied through gyrokinetic simulations that model high-frequency fluctuations measured in improved-confinement PPCD discharges. Linear simulations from two separate data sets were analyzed and the dominant instabilities were identified as density-gradient-driven TEM (for $\eta \approx 1.0$) and ITG (for $\eta \approx 1.5$). Nonlinear simulations with no external magnetic field perturbation to model tearing mode fluctuations produced turbulence in both cases with very strong zonal flows, and transport levels were well below the nominal experimental levels. An external, constant-in-time magnetic tearing perturbation was imposed in the simulations to model the effect of the residual tearing modes in PPCD discharges.

In both the TEM and ITG cases, this degraded the zonal structures, although with a different result in each case. For TEM, the transport was increased by orders of magnitude, reaching a value on the order of that expected from the experiment. However, the ITG transport was affected far less, increasing only by approximately a factor of two; future experimental analysis of the ITG discharge will allow for

proper comparison of transport quantities. The tearing perturbation also affected the energetic particle diffusivities, resulting in scaling behaviors that disagree with tokamak theory expectations, despite strong agreement without the perturbation.

Aspects of zonal flow physics in the tearing-free RFP were studied in detail to describe these observations. Zonal flows are found to be very sensitive to safety factor q , with the low- q regime of the RFP resulting in a much higher zonal flow residual than the tokamak; this provides a partial explanation for the strong zonal flow observed in the absence of magnetic tearing perturbations. Within this tearing-free regime, differences between the TEM and ITG case were addressed by looking at the effects of collisionality, as well as comparing the secondary instability dynamics. Collisionality was seen to have a role in setting TEM transport levels, with higher collisionalities resulting in an increased regime of TEM turbulence suppression by zonal flows; the ITG turbulence conversely showed very little dependence on collisionality. Observing secondary growth rates as a metric for nonlinear zonal flow excitation, the TEM zonal flow growth was observed to be more than twice that of the ITG for the discharges of interest. It was noted that the TEM zonal flows exhibit a preference for higher- k_x formation, which suggests that zonal flows in the TEM case are more effective at transferring energy out of unstable fluctuations.

These effects together serve to describe the observed turbulence behavior seen in the idealized, tearing-free regime of MST. For the regime in which the tearing effects are included, differences in saturation mechanism are observed for the TEM and ITG cases. Importantly, the ITG case is seen to depend fairly weakly upon zonal flows for saturation, in stark contrast to ITG modes in tokamaks for which zonal flows are the dominant saturation mechanism. This difference in behavior is attributed to the branch of ITG favored by the equilibrium; in this case the mode is shown to be more slab-like than the strongly toroidal ITG common in tokamaks. As such, the RFP ITG mode saturates through means other than zonal flows. It will be important for future model integration efforts to determine a self-consistent implementation of the tearing mode in PPCD, taking a step further than what has been done thus far. The inclusion of current gradients in the gyrokinetic distribution function, as well as accounting for the edge and core dynamics simultaneously in global Gene simulations, will be an important next step in this effort.

ACKNOWLEDGMENTS

The authors would like to thank J. R. Duff, J. S. Sarff, T. Nishizawa, and M. D. Nornberg for their valuable inputs concerning the experimental data from MST. The authors would also like to thank D.R. Ernst for the helpful discussions about collisional effects in TEM turbulence. This work is supported by the U.S. Department of Energy, Office of Science, Fusion Energy Sciences, under Award No. DE-FG02-85ER-53212, and by the National Science Foundation through XSEDE computing resources, allocation No. TG-PHY130027.

APPENDIX: TEARING PERTURBATION IMPLEMENTATION

Simulating discharges based on MST parameters using only self-consistently perturbed flux surfaces results in an unexpectedly low transport due to strong zonal flows. Those simulations do not take into account the tearing activity that remains in the plasma, albeit at a reduced level because of PPCD. To more accurately model transport in these discharges, the effect of residual tearing on zonal flows must be taken into account. This is done here by including a constant-in-time resonant A_{\parallel} perturbation. The details of the implementation, adapted from Refs. 9 and 48, are discussed in what follows. Beginning with Ampere's Law

$$k_{\perp}^2 A_{\parallel}^{\text{sc}} = j_{\parallel} = \frac{\beta}{2} \sum_j q_j n_{j0} v_{Tj} \pi B_0 \int v_{\parallel} J_0(\lambda_j) f_j(k) dv_{\parallel} d\mu, \quad (\text{A1})$$

where $f_j = g_j - (q_j v_{Tj} v_{\parallel} F_{j0} / T_{j0}) A_{\parallel}$ is the distribution function of species j , while β is the ratio of plasma pressure to magnetic field pressure, q_e is electron charge, B_0 is the background magnetic field, v_{\parallel} is the velocity parallel to the magnetic field, μ is the magnetic moment, J_0 is the zeroth-order Bessel function, and $\lambda_j \equiv \left(\sqrt{2B_0\mu/m_j} \right) k_{\perp} / \Omega_j$. To include the tearing perturbation, one may add an external perturbation $A_{\parallel}^{\text{ext}}$ to the self-consistent $A_{\parallel}^{\text{sc}}$, such that $A_{\parallel} \rightarrow A_{\parallel}^{\text{sc}}(k_x, k_y, z, t) + A_{\parallel}^{\text{ext}}(0, k_y, \min, z)$. Plugging this perturbed distribution function f_j into Eq. (A1), one obtains

$$k_{\perp}^2 A_{\parallel}^{\text{sc}} = \frac{\beta}{2} \sum_j q_j n_{j0} v_{Tj} \pi B_0 \int v_{\parallel} J_0(\lambda_j) \times \left(g_j - q_j v_{\parallel} v_{Tj} \frac{F_{j0}}{T_{j0}} (A_{\parallel}^{\text{sc}} + A_{\parallel}^{\text{ext}}) \right) dv_{\parallel} d\mu. \quad (\text{A2})$$

This equation can be solved for $A_{\parallel}^{\text{sc}}$

$$A_{\parallel}^{\text{sc}} = \frac{\frac{\beta}{2} \sum_j q_j n_{j0} v_{Tj} \pi B_0 \int v_{\parallel} J_0(\lambda) g dv_{\parallel} d\mu}{k_{\perp}^2 + I_1} + \frac{I_1}{k_{\perp}^2 + I_1} A_{\parallel}^{\text{ext}}, \quad (\text{A3})$$

where

$$I_1 \equiv \sum_j \frac{\beta}{2T_{j0}} q_j^2 n_{j0} v_{Tj}^2 \pi B_0 \int J_0(\lambda) v_{\parallel}^2 F_{j0} dv_{\parallel} d\mu. \quad (\text{A4})$$

The first term on the right-hand-side of E. (A3) represents the standard picture of A_{\parallel} evolution without any perturbation, taken from Ampere's law; the second term is the contribution of an externally imposed perturbation. Note that Ref. 9 neglected the prefactor on the second term in Eq. (A3). The functional form of the tearing-parity perturbation is implemented as a Gaussian in the z direction (parallel to the background magnetic field), $A_{\parallel}^{\text{ext}} = A_0 e^{-z^2}$. The global tearing mode cascade extends to spatial scales relevant to microturbulence, but it is assumed here that the cascade is sufficiently steep so that the tearing fluctuation can be

included only at the largest scales of the simulation box, ($k_x = 0, k_y = 2\pi/L_y$), corresponding to a purely radial fluctuation in the magnetic field. The value chosen for the amplitude of the perturbation is informed from the experimental measurements: high- n B_{ϕ} and B_{θ} fluctuations are measured outside the reversal surface, and B_r is determined relative to these via the tearing eigenfunction solver RESTER.⁴⁹

- ¹D. R. Ernst, P. T. Bonoli, P. J. Catto, W. Dorland, C. L. Fiore, R. S. Granetz, M. Greenwald, A. E. Hubbard, M. Porkolab, M. H. Redi, J. E. Rice, and K. Zhurovich, and Alcator C-Mod Group, *Phys. Plasmas* **11**, 2637 (2004).
- ²D. Told, F. Jenko, T. Görler, F. J. Casson, E. Fable, and ASDEX Upgrade Team, *Phys. Plasmas* **20**, 122312 (2013).
- ³T.-H. Watanabe, H. Sugama, and S. Ferrando-Margalet, *Phys. Rev. Lett.* **100**, 195002 (2008).
- ⁴B. J. Faber, M. J. Pueschel, J. H. E. Proll, P. Xanthopoulos, P. W. Terry, C. C. Hegna, G. M. Weir, K. M. Likin, and J. N. Talmadge, *Phys. Plasmas* **22**, 072305 (2015).
- ⁵P. Helander, T. Bird, F. Jenko, R. Kleiber, G. G. Plunk, J. H. E. Proll, J. Riemann, and P. Xanthopoulos, *Nucl. Fusion* **55**, 053030 (2015).
- ⁶V. Tangri, P. W. Terry, and R. E. Waltz, *Phys. Plasmas* **18**, 052310 (2011).
- ⁷D. Carmody, M. J. Pueschel, and P. W. Terry, *Phys. Plasmas* **20**, 052110 (2013).
- ⁸I. Predebon and F. Sattin, *Phys. Plasmas* **20**, 040701 (2013).
- ⁹D. Carmody, M. J. Puseschel, J. K. Anderson, and P. W. Terry, *Phys. Plasmas* **22**, 012504 (2015).
- ¹⁰I. Predebon and P. Xanthopoulos, *Phys. Plasmas* **22**, 052308 (2015).
- ¹¹Z. Lin, T. S. Hahm, W. W. Lee, W. M. Tang, and R. B. White, *Phys. Plasmas* **7**, 1857 (2000).
- ¹²P. H. Diamond, S.-I. Itoh, K. Itoh, and T. S. Hahm, *Plasma Phys. Controlled Fusion* **47**, R35 (2005).
- ¹³B. Scott, *New J. Phys.* **7**, 92 (2005).
- ¹⁴M. J. Pueschel and F. Jenko, *Phys. Plasmas* **17**, 062307 (2010).
- ¹⁵H. Biglari, P. H. Diamond, and P. W. Terry, *Phys. Fluids B* **2**, 1 (1990).
- ¹⁶K. D. Makwana, P. W. Terry, and J.-H. Kim, *Phys. Plasmas* **19**, 062310 (2012).
- ¹⁷K. D. Makwana, P. W. Terry, M. J. Pueschel, and D. R. Hatch, *Phys. Rev. Lett.* **112**, 095002 (2014).
- ¹⁸P. W. Terry, M. J. Pueschel, D. Carmody, and W. M. Nevins, *Phys. Plasmas* **20**, 112502 (2013).
- ¹⁹M. J. Pueschel, D. R. Hatch, T. Görler, W. M. Nevins, F. Jenko, P. W. Terry, and D. Told, *Phys. Plasmas* **20**, 102301 (2013).
- ²⁰J. S. Sarff, S. A. Hokin, H. Ji, S. C. Prager, and C. R. Sovinec, *Phys. Rev. Lett.* **72**, 3670 (1994).
- ²¹B. E. Chapman, A. F. Almagri, J. K. Anderson, D. L. Brower, K. J. Caspary, D. J. Clayton, D. Craig, D. J. Den Hartog, W. X. Ding, D. A. Ennis, G. Fiksel, S. Gangadhara, S. Kumar, R. M. Magee, R. O'Connell, E. Parke, S. C. Prager, J. A. Reusch, J. S. Sarff, H. D. Stephens, and Y. M. Yang, *Plasma Phys. Controlled Fusion* **52**, 124048 (2010).
- ²²T. Hauff, M. J. Pueschel, T. Dannert, and F. Jenko, *Phys. Rev. Lett.* **102**, 075004 (2009).
- ²³J. R. Duff, Z. R. Williams, D. L. Brower, B. E. Chapman, W. X. Ding, M. J. Pueschel, J. S. Sarff, and P. W. Terry, "Observation of trapped-electron-mode microturbulence in reversed field pinch plasmas," *Phys. Plasmas* (submitted).
- ²⁴T. Nishizawa, M. D. Nornberg, D. J. Den Hartog, and D. Craig, *Rev. Sci. Instrum.* **87**, 11E530 (2016).
- ²⁵F. Jenko, W. Dorland, M. Kotschenreuther, and B. N. Rogers, *Phys. Plasmas* **7**, 1904 (2000).
- ²⁶See <http://www.genecode.org> for code details and access.
- ²⁷X. Lapillonne, S. Brunner, T. Dannert, S. Jolliet, A. Marinoni, L. Villard, T. Görler, F. Jenko, and F. Merz, *Phys. Plasmas* **16**, 032308 (2009).
- ²⁸J. K. Anderson, C. B. Forest, T. M. Biewer, J. S. Sarff, and J. C. Wright, *Nucl. Fusion* **44**, 162 (2004).
- ²⁹G. Rewoldt and W. M. Tang, *Phys. Fluids B: Plasma Phys.* **2**, 318 (1990).
- ³⁰B. Coppi and F. Pegoraro, *Nucl. Fusion* **17**, 969 (1977).
- ³¹A. M. Dimits, G. Bateman, M. A. Beer, B. I. Cohen, W. Dorland, G. W. Hammett, C. Kim, J. E. Kinsey, M. Kotschenreuther, A. H. Kritiz, L. L. Lao, J. Mandrekas, W. M. Nevins, S. E. Parker, A. J. Redd, D. E. Shumaker, R. Sydora, and J. Weiland, *Phys. Plasmas* **7**, 969 (2000).
- ³²W. Horton, D.-I. Choi, and W. M. Tang, *Phys. Fluids* **24**, 1077 (1981).

- ³³P. W. Terry, D. A. Baver, and D. R. Hatch, *Phys. Plasmas* **16**, 122305 (2009).
- ³⁴C. Holland, P. H. Diamond, S. Champeaux, E. Kim, O. Gurcan, M. N. Rosenbluth, G. R. Tynan, N. Crocker, W. Nevins, and J. Candy, *Nucl. Fusion* **43**, 761 (2003).
- ³⁵C. C. Hegna, P. W. Terry, and B. J. Faber, "Theory of ITG turbulent saturation in stellarators: identifying mechanisms to reduce turbulent transport," *Phys. Plasmas* (submitted).
- ³⁶P. W. Terry, D. Carmody, H. Doerk, W. Guttenfelder, D. R. Hatch, C. C. Hegna, A. Ishizawa, F. Jenko, W. M. Nevins, I. Predebon, M. J. Pueschel, J. S. Sarff, and G. G. Whelan, *Nucl. Fusion* **55**, 104011 (2015).
- ³⁷H. Sugama and T.-H. Watanabe, *Phys. Plasmas* **13**, 012501 (2006).
- ³⁸M. N. Rosenbluth and F. L. Hinton, *Phys. Rev. Lett.* **80**, 724 (1998).
- ³⁹S. C. Cowley, R. M. Kulsrud, and R. Sudan, *Phys. Fluids B* **3**, 2767 (1991).
- ⁴⁰B. N. Rogers, W. Dorland, and M. Kotschenreuther, *Phys. Rev. Lett.* **85**, 5336 (2000).
- ⁴¹D. R. Ernst, N. Basse, W. Dorland, C. L. Fiore, L. Lin, A. Long, M. Porkolab, K. Zeller, and K. Zhurovich, in *Proceedings of the 21st IAEA Fusion Energy Conference, Chengdu, China* (2006), paper No. IAEA-CN-149/TH/1-3.
- ⁴²M. J. Pueschel, T. Görler, F. Jenko, D. R. Hatch, and A. J. Cianciara, *Phys. Plasmas* **20**, 102308 (2013).
- ⁴³W. W. Heidbrink, J. M. Park, M. Murakami, C. C. Petty, C. Holcomb, and M. A. Van Zeeland, *Phys. Rev. Lett.* **103**, 175001 (2009).
- ⁴⁴D. C. Pace, M. E. Austin, E. M. Bass, R. V. Budny, W. W. Heidbrink, J. C. Hillesheim, C. T. Holcomb, M. Gorelenkov, B. A. Grierson, D. C. McCune, G. R. McKee, C. M. Muscatello, J. M. Park, C. C. Petty, T. L. Rhodes, G. M. Staebler, T. Suzuki, M. A. Van Zeeland, R. E. Waltz, G. Wang, A. E. White, Z. Yan, X. Yuan, and Y. B. Zhu, *Phys. Plasmas* **20**, 056108 (2013).
- ⁴⁵M. Nocente, M. Albergante, J. Eriksson, S. Conroy, G. Ericsson, D. Farina, C. Hellesten, J. Källne, S. Popovichev, M. Tardocchi, G. Gorini, and JET-EFDA Contributors, *Nucl. Fusion* **54**, 104010 (2014).
- ⁴⁶B. Geiger, M. Weiland, A. S. Jacobsen, D. Rittich, R. Dux, R. Fischer, C. Hopf, M. Maraschek, R. M. McDermott, S. K. Nielsen, T. Odstrcil, M. Reich, F. Ryter, M. Salewski, P. A. Schneider, G. Tardini, and the ASDEX Update Team, *Nucl. Fusion* **55**, 083001 (2015).
- ⁴⁷M. J. Pueschel, F. Jenko, M. Schneller, T. Hauff, S. Günter, and G. Tardini, *Nucl. Fusion* **52**, 103018 (2012).
- ⁴⁸A. Bañón Navarro, L. Bardóczi, T. A. Carter, F. Jenko, and T. L. Rhodes, *Plasma Phys. Controlled Fusion* **59**, 034004 (2017).
- ⁴⁹C. Sovinec, Ph.D. thesis, University of Wisconsin-Madison, 1995.